

# International Journal of Nanoelectronics and Materials

IJNeaM -

ISSN 1985-5761 | E-ISSN 2232-1535



# Comparative simulation study of polymeric buffer layer incorporated CuI-based HTM for perovskite solar cells

Thaddeus Lee a,b, Chun Hui Tan a,b, Chai Yan Ng b,c, M.A. Islam d,e,f, Hing Wah Lee g, Chun Hong Voon h, Foo Wah Low a,b\*

- <sup>a</sup> Department of Electrical and Electronic Engineering, Lee Kong Chian Faculty of Engineering and Science, Universiti Tunku Abdul Rahman, 43000 Kajang, Selangor, Malaysia
- <sup>b</sup> Centre for Advanced and Sustainable Materials Research (CASMR), Lee Kong Chian Faculty of Engineering and Science, Universiti Tunku Abdul Rahman, 43000 Kajang, Selangor, Malaysia
- <sup>c</sup> Department of Mechanical and Material Engineering, Lee Kong Chian Faculty of Engineering and Science, Universiti Tunku Abdul Rahman, 43000 Kajang, Selangor, Malaysia
- d Department of Electrical Engineering, Faculty of Engineering, University of Malaya, Kuala Lumpur, 50603, Malaysia
- e Centre of Printable Electronics, Universiti Malaya, 50603 Kuala Lumpur
- f Miyan Research Institute. International University of Business Agriculture and Technology (IUBAT), Dhaka, 1230, Bangladesh
- g Semiconductor and Venture Division, Selangor Information Technology & Digital Economy Corporation (SIDEC), 40000 Shah Alam, Selangor, Malaysia
- h Institute of Nano Electronic Engineering, Universiti Malaysia Perlis, Kangar, Malaysia
- \* Corresponding author: lowfw@utar.edu.my

Received 26 June 2024, Revised 21 January 2025, Accepted 10 February 2025

#### **ABSTRACT**

The commercial implementation of perovskite solar cells (PSCs) with inorganic hole-transporting materials (HTMs) is hindered by the requirement for more complex synthesis and processing methods. This study provides insights into the incorporation of buffer layers in copper iodide (CuI)-based perovskite solar cells through comparative simulation work. The result shows that the poly-TPD buffer layer outperforms other buffer layers, such as PMMA, P3HT, PTAA, and spiro-OMeTAD, achieving an open-circuit voltage ( $V_{oc}$ ) of 1.2687 V, short-circuit current density ( $J_{sc}$ ) of 24.4410 mA/cm², fill factor (FF) of 83.8048%, and power conversion efficiency (PCE) of 25.9855%, which is comparable to the performance of a device without a buffer layer. This superiority is mainly attributed to the compatibility of the energy level alignment. In addition, the ability of the buffer layer materials to dissolve in solvents without negatively impacting the crystalline properties of the perovskite layer opens up possibilities for fabricating solution-processed PSCs with inorganic HTMs. The research highlights the significance of electron affinity, band gap, hole mobility, and interface defect density of the buffer layer material in determining device performance. Furthermore, it was observed that the improvements brought about by optimizing these factors individually reached a saturation point. Therefore, a holistic approach that considers the interplay between these factors is necessary to further enhance device performance in PSCs.

Keywords: Numerical Simulation; Hole Transporting Material; Buffer Layer; Perovskite Solar Cell

### 1. INTRODUCTION

Lead halide PSCs are a relatively low-cost photovoltaic technology that is comparable in quality to other wellestablished technologies such as silicon, GaAs, and CdTebased solar cells [1]. Generally, the perovskite compound serves as the core component to enable light harvesting in the active layer. PSCs have been widely used in space applications, photovoltaic-driven catalysis, integrated tandem solar cells, and energy storage systems [2]. These perovskites often contain a hybrid of organic-inorganic lead or tin-halide material as the absorbing layer. [3]. Solution-processed hybrid organic-inorganic perovskite devices have shown longer carrier diffusion lengths and good optical properties, resulting in high device efficiency [4]. In recent years, the efficiency of PSCs in practical applications has increased from 3.8% to 25.5%, demonstrating impressive optical and electrical properties [5]. Emerging PSCs are expected to enter specific market segments of photovoltaics (PV), such as buildingintegrated PV, in the coming years as device fabrication

scales up and device longevity improves. However, PSCs still suffer from poor stability due to film defects, high solar thermal effects, illumination issues, and inadequate applied electric fields [6].

HTM is a crucial component that requires additional research to enhance the performance and stability of PSCs. At present, the small molecule spiro-OMeTAD is frequently utilized as the solid-state HTM in PSCs and has garnered significant attention over the past decade [7]. However, spiro-OMeTAD has its shortcomings, including a complicated synthesis route, high production cost, and a requirement for hygroscopic dopants to boost charge-carrier mobility. These requirements indirectly limit the large-scale applications of spiro-OMeTAD [8]. In fact, there has been a growing interest in substituting spiro-OMeTAD with inorganic HTMs that promise lower cost, better thermal stability, and more effective hole extraction [9]. One class of inorganic HTMs that has received significant attention is copper-based compounds. They have been

widely studied in numerous simulation studies due to their more favorable energy alignment with perovskite compared to spiro-OMeTAD [10].

The methods for depositing copper-based HTM in PSCs are not well-discussed, despite the promising performance output that can be achieved by using them. These HTMs are hard to dissolve in non-polar solvents, which are necessary to maintain the perovskite layer. Unfortunately, using these HTMs in inverted perovskite devices may also cause damage to the formed inorganic HTMs by the perovskite solutions. Furthermore, simulation studies have found that copper (I) oxide, or Cu<sub>2</sub>O, is the best alternative to spiro-OMeTAD. However, it has the drawback of being insoluble in non-polar solvents, which hinders solution processing [11]. To avoid damaging the perovskite layer, Cu<sub>2</sub>O may need to be separately prepared in the form of nanoparticles. However, this process may encounter issues with dispersion and homogeneity, or require the use of more equipment-dependent methods such as ion beam sputtering [12].

Interestingly, copper iodide (CuI) has shown promising simulation results. Replacing the HTM with CuI vielded competitive results compared to existing models [13]. It can fully dissolve in acetonitrile (ACN). Still, ACN is a polar aprotic solvent of high dipole moment that can corrode perovskite films and negatively impact the PSC efficiency and durability [14]. Researchers have explored various approaches to fabricating PSCs using CuI as the HTM. Srivastava et al. created a PSC by spin-coating CuI solution in ACN, achieving a PCE of 13.64% despite potential negative effects on the absorber layer morphology [15]. Sun et al. developed an inverted planar heterojunction solar cell using CuI as the HTM, reaching a PCE of 16.8%. This success was attributed to optimized perovskite morphology and the CuI layer being deposited first on the transparent conductive electrode, mitigating issues with the ACN solution [16]. In another study, Srivastava et al. employed a transfer printing process to apply CuI stamps onto prepared perovskite layers, avoiding ACN's effects. They achieved a promising PCE of 8.3%, though slightly lower than reference PSCs using spin-coated spiro-OMeTAD HTM. This difference may stem from defects in the CuI HTL caused by stress and mechanical failures during the transfer-printing process [17].

To further improve the implementation of CuI-based HTMs in planar n-i-p structure PSCs, it is proposed in this study to deposit a layer of another HTM that is dissolved in nonpolar solvents. This will protect the perovskite layer from the harmful effects of HTM deposition, and the HTM layer from similar effects from perovskite deposition in the case of inverted structure perovskite devices. To address this issue, it is proposed to apply a layer of another material (HTM) that is dissolved in non-polar solvents. This layer will protect the perovskite layer from the harmful effects of HTM deposition. Similarly, it will protect the HTM layer from the negative effects of perovskite deposition in the case of inverted structure perovskite devices.

An extensive comparative simulation analysis was conducted to examine the efficiency performance of various buffer layers placed between the perovskite layer and the CuI layer. Initially, buffer layer-free CuI-based PSCs were simulated, optimized, and used as a benchmark for performance comparisons. Various buffer layer materials, such as PMMA, P3HT, poly-TPD, PTAA, and spiro-OMeTAD, were selected for the comparative analysis. While buffer layers are used to lessen the detrimental effects of HTM deposition on the perovskite layer, they do not enhance the device's performance compared to a device without a buffer layer from a computational standpoint. This study aims to identify the buffer layer that has the least impact on the device's efficiency, so that better-performing devices may be fabricated in practice. Additionally, this study addresses the potential factors that contribute to poor electrical performance.

#### 2. METHODOLOGY

### 2.1. Buffer Layer Materials Used and Respective Solvents

Poly(methyl methacrylate) (PMMA), Poly(3-hexylthiophene) (P3HT), Poly(4-butyl-N,N-diphenylaniline) (Poly-TPD), Poly(triarylamine) (PTAA), and 2,2',7,7'-Tetrakis[N,N-di(4-methoxyphenyl)amino]-9,9'-spirobifluorene (spiro-OMeTAD) are chosen as the deposition layer materials between CuI and perovskite for the simulation studies.

The solvents used to dissolve materials such as CuI or HTMs in perovskite solar cells can have deleterious effects on the methylammonium lead iodide (MALI) perovskite layer. Depending on the ability of solvents to dissolve or react with perovskite material, they can potentially degrade the annealed perovskite layer, leading to reduced device performance. Thus, it's essential to consider the properties of the solvent when designing and optimizing perovskite solar cells.

### 2.2 Simulation Software and Device Architecture

SCAPS-1D is a one-dimensional solar cell device simulator, freely available to the photovoltaic (PV) research community [18]. Developed at ELIS, University of Gent, it is a reliable software that solves the three fundamental semiconductor equations: the Poisson equation, and the continuity equations for electrons and holes [19]. These equations, represented as Eqs. (1) - (3) are calculated under steady-state conditions in one dimension.

$$\frac{d^2}{dx^2}\psi(x) = \frac{e}{\varepsilon_0\varepsilon_r} \Big( p(x) - n(x) + N_D - N_A + \rho_p - \rho_n \Big) \quad (equation \ 1)$$

Here,  $\psi$  represents the electrostatic potential, e stands for electrical charge,  $\epsilon_r$ , and  $\epsilon_0$  denote the relative and vacuum dielectric permittivity, respectively. p and n are the concentrations of holes and electrons, respectively, while

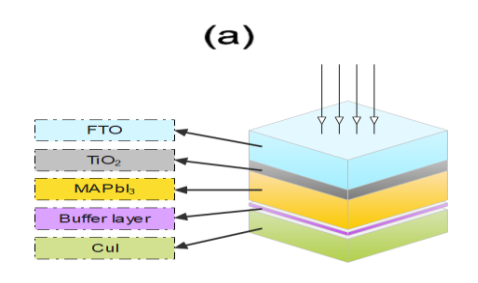
 $N_D$  and  $N_A$  symbolize the donor and acceptor densities, respectively. Lastly,  $\rho_p$  and  $\rho_n$  are the distributions of holes and electrons, respectively.

$$\frac{dJ_n}{dx} = G - R \quad (equation 2)$$

$$\frac{dJ_p}{dx} = G - R \quad (equation 3)$$

Where  $J_n$  and  $J_p$  are the electron and hole current densities, R and G are the recombination rate and generation rate, respectively [20]. The SCAPS-1D software has shown consistency between its simulation results experimental results in various literature. For example, Yadav et al. reported that the current-voltage result and external quantum efficiency (EQE) result of their simulated and fabricated device were in good agreement with each other [21]. Abdelaziz et al. also reported that simulation using SCAPS gave expected results and confirmed experimental data, save for the lower value of bulk heterojunction collection efficiency [22]. It can be expected that the performance of an experimental device will fall behind that of a simulated one despite the results being in good agreement. This can be attributed to non-idealities such as the instability of materials/chemicals in the fabricated device due to moisture [23], and other defects or imperfections not considered during simulation. To ensure a good match between experimental and simulation results, calibration is needed. Therefore, this study provides only a qualitative comparison between buffer layer materials, and the simulated values may be overrated in practice. Nonetheless, the SCAPS-1D simulator can reliably model one-dimensional solar cells. A strong correlation between simulated and experimental devices can enhance the understanding of the solar cell's charge transport mechanisms and power conversion efficiency.

The simulated solar cell used for performance evaluation follows the n-i-p planar structure, with illumination occurring from the ETL side. The cell's configuration is ordered as follows: FTO glass (TCO)/TiO<sub>2</sub> (ETL)/MAPbI<sub>3</sub> (absorber)/varied buffer layer/CuI (HTM). Figure 1(a)-(b) presents the schematic diagram of the simulated devices and their energy band diagrams. Tables 2 and 3 list the basic parameters of the materials used. The simulations were conducted under the AM1.5G solar radiation spectrum. The perovskite is placed between the ETL and HTM layers, with the buffer layer acting as a protective barrier to maintain the perovskite's quality and crystallinity.



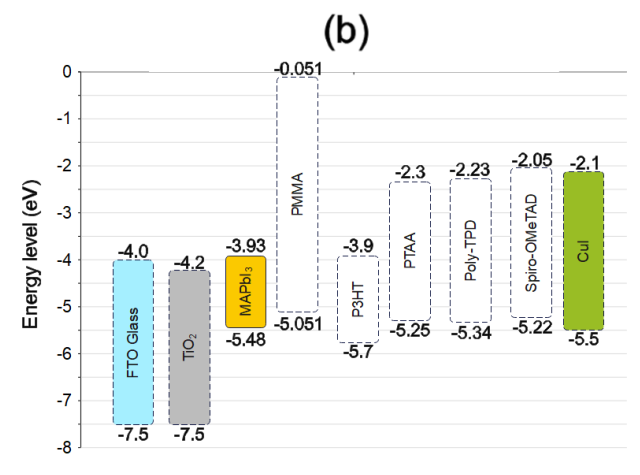


**Figure 1. (a)** Schematic illustration of the simulated device, and **(b)** energy band diagram of materials.

**Table 1.** Simulation parameters of PSCs.

Material Properties	TCO (FTO) [24]	ETL (TiO <sub>2</sub> ) [25]	Absorber (MAPbI <sub>3</sub> ) [25]	HTM (CuI) [26]	PMMA	P3HT [30]	PTAA [31]	Poly- TPD [32]	Spiro- OMeTAD
Thickness (µm)	0.5	0.05	0.5	0.05	0.015	0.015	0.015	0.015	0.015
Eg (eV)	3.5	3.3	1.55	3.4	5.01 [27]	1.8	2.95	3.11	3.17 [33]
χ (eV)	4	4.2	3.93	2.1	0.051 [28]	3.9	2.3	2.23	2.05 [33]
$\epsilon_{r}$	9	9	6.5	10	3.64 [29]	3	9	3	3 [33]
Nc (cm³)	2 × 10 <sup>18</sup>	1 × 10 <sup>19</sup>	$2.2 \times 10^{18}$	2.5 × 10 <sup>18</sup>	2.8 × 10 <sup>19</sup>	2.5 × 10 <sup>18</sup>	2.8 × 10 <sup>19</sup>	2.8 × 10 <sup>19</sup>	$2.8 \times 10^{19}$
Nv (cm³)	1.8 × 10 <sup>18</sup>	1 × 10 <sup>19</sup>	$1.8 \times 10^{19}$	1.8 × 10 <sup>19</sup>	1 × 10 <sup>19</sup>	1.8 × 10 <sup>19</sup>	1 × 10 <sup>19</sup>	1 × 10 <sup>19</sup>	1 × 10 <sup>19</sup>
vn (cm.s <sup>-1</sup> )	1 × 10 <sup>7</sup>	1 × 10 <sup>7</sup>	1 × 10 <sup>7</sup>	1 × 10 <sup>7</sup>	1 × 10 <sup>7</sup>	1 × 10 <sup>7</sup>	1 × 10 <sup>7</sup>	1 × 10 <sup>7</sup>	1 × 10 <sup>7</sup>
v <sub>h</sub> (cm.s <sup>-1</sup> )	1 × 10 <sup>7</sup>	1 × 10 <sup>7</sup>	$1 \times 10^7$	1 × 10 <sup>7</sup>	$1 \times 10^7$	1 × 10 <sup>7</sup>	1 × 10 <sup>7</sup>	1 × 10 <sup>7</sup>	1 × 10 <sup>7</sup>
$\mu_n/\mu_h(cm^2 V^{-1}s^{-1})$	20/10	0.02/2	0.5/0.5	2 × 10 <sup>4</sup> /2 × 10 <sup>4</sup>	10-4/10-	10 <sup>-</sup> 4/10 <sup>-4</sup>	1/40	10 <sup>-</sup> 4/10 <sup>-4</sup>	2 × 10 <sup>-4</sup> /2 × 10 <sup>-4</sup> [34]
Np (cm <sup>-3</sup> )	2 × 10 <sup>19</sup>	5 × 10 <sup>19</sup>	-	-	-	-	-	-	-
N <sub>A</sub> (cm <sup>-3</sup> )	-	-	$1 \times 10^{15}$	1 × 10 <sup>20</sup>	1 × 10 <sup>18</sup>	1 × 10 <sup>18</sup>	1 × 10 <sup>18</sup>	1 × 10 <sup>18</sup>	1 × 10 <sup>18</sup>
N <sub>t</sub> (cm <sup>-3</sup> )	1 × 10 <sup>15</sup>	1 × 10 <sup>15</sup>	1 × 10 <sup>12</sup>	1 × 10 <sup>14</sup>	1 × 10 <sup>12</sup>	1 × 10 <sup>12</sup>	1 × 10 <sup>12</sup>	1 × 10 <sup>12</sup>	1 × 10 <sup>12</sup>
Et (eV) above Ev	0.6	0.6	0.7	0.1	0.1	0.1	0.1	0.1	0.1
Capture cross section electrons (cm <sup>2</sup> )	2 × 10 <sup>-15</sup>	1 × 10 <sup>-15</sup>	2 × 10 <sup>-14</sup>	1 × 10 <sup>-15</sup>	1 × 10 <sup>-</sup>	1 × 10 <sup>-15</sup>	1 × 10 <sup>-15</sup>	1 × 10 <sup>-15</sup>	1 × 10 <sup>-15</sup>
Capture cross section holes (cm <sup>2</sup> )	2 × 10 <sup>-15</sup>	1 × 10 <sup>-15</sup>	2 × 10 <sup>-14</sup>	1 × 10 <sup>-15</sup>	1 × 10 <sup>-</sup>	1 × 10 <sup>-15</sup>	1 × 10 <sup>-15</sup>	1 × 10 <sup>-15</sup>	1 × 10 <sup>-15</sup>

Table 2. Interface defect properties panel

Defect type	Neutral
Capture cross section electrons (cm <sup>2</sup> )	10-19
Capture cross section hole (cm <sup>2</sup> )	10-19
Energetic distribution	Single
Reference for defect energy level Et	Above the highest E <sub>V</sub>
Energy level with respect to reference (eV)	0.6
Characteristic energy (eV)	0.1
Total density (integrated over all energies) (cm <sup>-2</sup> )	$10^{10}$

Throughout all the simulations performed, four photovoltaic parameters will be presented:  $V_{oc}$ ,  $J_{sc}$ , FF, and PCE. To assess the performance of the cell, the performance parameters are plotted as each material value is simulated [35].

 $V_{oc}$  = maximum voltage that can be measured from a solar cell when no current flows through its terminals.

 $J_{sc}$  = current that flows through a solar cell when short-circuited without a load and at zero voltage.

 $V_{mpp}$  = Voltage at the maximum power point

 $J_{mpp}$  = Current at the maximum power point

*FF* = Efficiency metric measuring how closely a solar cell approaches its maximum power output.

PCE = Ratio of electrical power output to incident solar power in a solar cell.

FF and PCE are calculated using the following equations:

$$FF = \frac{J_{mpp} \cdot V_{mpp}}{J_{SC} \cdot V_{OC}} = \frac{P_{max}}{J_{SC} \cdot V_{OC}} \quad (equation \ 4)$$

$$PCE = \frac{P_{max}}{P_{in}} = \frac{FF \cdot V_{OC} \cdot J_{SC}}{P_{in}} \quad (equation 5)$$

### 3. RESULTS AND DISCUSSION

### Optimum buffer layer material identification

To identify the best buffer layer material for an efficient copper iodide-based PSC, the photovoltaic parameters were simulated using different buffer layers, including the polymers PMMA, P3HT, poly-TPD, PTAA, and small molecule spiro-OMeTAD. During the modeling of various buffer layers, the parameters for the ETM, HTM, and perovskite layers were kept constant. To ensure consistency in the analysis, identical values for both bulk and interface defect densities were used. The J-V characteristic curves and EQEs of the simulated PSCs are displayed in Figure 2(a)-(b).

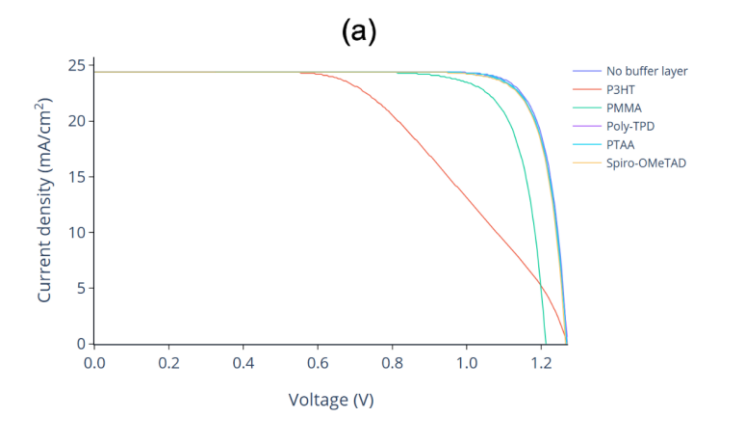
The photovoltaic metrics of the simulated devices are detailed in Table 4. The simulation results suggest that changes to the buffer layer parameters, as listed in Table 2, affected the photovoltaic metrics, specifically the  $V_{oc}$  and FF. These changes are evident in Figure 2(a) and Table 4.

Notably, the PSCs featuring the P3HT and PMMA buffer layers delivered a reduction in *FF* and PCE, especially in the case of P3HT. This can be attributed to a mismatch between the valence bands of P3HT and PMMA, and the valence bands of copper iodide and perovskite material, which contributed to an energy barrier to be surmounted by the photogenerated carriers.

In the case of P3HT, the valence band maximum (VB<sub>max</sub> = 5.70 eV) is somewhat deeper or has a larger value than the perovskite and HTM. On the other hand, PMMA has a shallower, or smaller valence band maximum (VB<sub>max</sub> = 5.061 eV) compared to the perovskite and HTM. Despite these differences, an energy barrier impeding the efficient transfer of holes from the perovskite to HTM is observed in both simulations.

**Table 3.** Photovoltaic parameters from simulations of PSCs with various buffer layers.

Parameters	Voc (V)	J <sub>sc</sub> (mA.cm <sup>-2</sup> )	FF (%)	PCE (%)
No buffer layer	1.2700	24.4409	84.2889	26.1642
PMMA	1.2124	24.4414	80.2558	23.7829
РЗНТ	1.2704	24.4467	53.2223	16.5286
Poly-TPD	1.2687	24.4410	83.8048	25.9855
PTAA	1.2673	24.4409	83.6100	25.8967
Spiro-OMeTAD	1.2659	24.4414	83.4290	25.8136



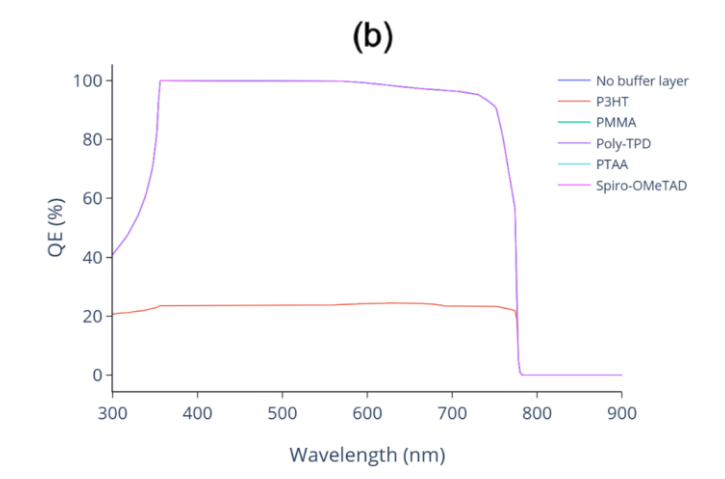


**Figure 2.** (a) J-V curves, and (b) EQEs of the simulated PSCs.

The loss of FF and PCE indicates the formation of an energy barrier between the HTM, buffer layer, and absorber layer around the maximum power point of the simulated device. In the case of poly-TPD, PTAA, and spiro-OMeTAD, the devices exhibited performance parameters similar to the reference device without a buffer layer, with the poly-TPD device having superior performance parameters. The sustained performance can be attributed to the correct alignment of energy levels, appropriate electron affinity values, and suitable band gaps of the simulated materials. Likewise, the EOEs of the simulated PSCs show minor variations. However, the P3HT device stands out with a significantly reduced EQE due to inefficient charge transfer characteristics. In Figure 2(b), the P3HT device (orange) demonstrates a noticeably lower EQE compared to the other buffer layers. This is represented as a separate line in the figure, while the EQEs of the remaining buffer layers are stacked behind the EQE of the poly-TPD device (purple).

Although the buffer layer materials used in this study are costly, except for PMMA, which did not result in the best performance parameters for the solar cell, the cost of these materials will not be factored into this simulation study, which only employs a very thin layer of material. Therefore, poly-TPD is the chosen buffer layer material for this specific solar cell configuration. In fact, the suitability of each buffer layer material highly depends on the semiconductor parameters of the HTM and perovskite layer.

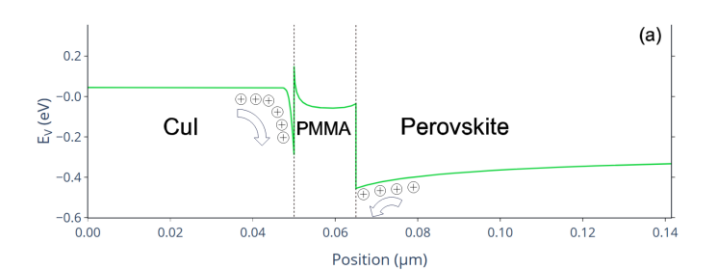
The simulation results align well with prior experimental work, further supporting the choice of poly-TPD as the buffer layer in CuI-based perovskite solar cells. Previous experimental studies demonstrated significant improvements in solar cell efficiency when poly-TPD was employed in solution-processed perovskite solar cells. These enhancements were primarily attributed to improved perovskite film morphology, which led to more efficient charge transfer mechanisms [36, 37].

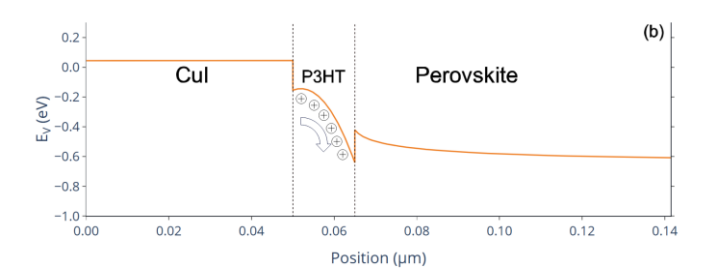
The critical role of energy level alignment is particularly noteworthy. The highest occupied molecular orbital (HOMO) level of poly-TPD aligns well with the valence band level of the perovskite layer [38]. This alignment facilitates efficient hole transfer while minimizing energy losses at the interface—a finding supported by this study's simulation results. The superior performance of poly-TPD observed in both simulations and experiments can therefore be attributed to its optimal energy level compatibility with the active and transport layers.

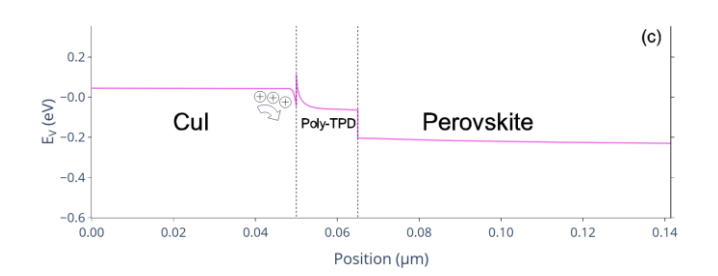
## Electron affinity, band gap of the buffer layer, and PSC performance

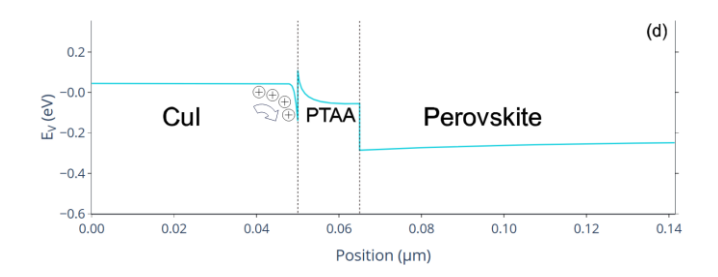
Efficient flow of holes from the perovskite to the buffer layer, to the HTM requires proper alignment of the valence bands of the two materials [39]. Similarly, the conduction bands of the perovskite and ETL should align to facilitate

electron transport [40]. This proper alignment helps to prevent energy barriers and internal voltage drops (IVD), both of which are crucial for improving the  $V_{oc}$  values of the PSCs. The energy band matching between buffer layers and the perovskite layer can be observed by analyzing the energy band levels of the simulated PSCs, as illustrated in Figure 3.









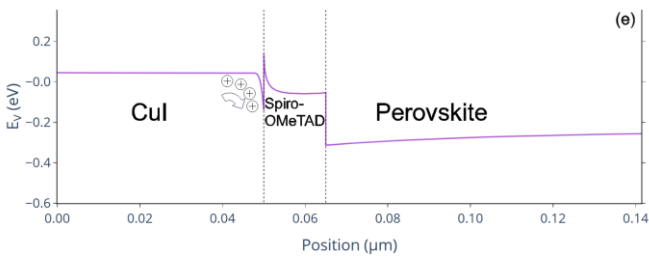


**Figure 3**. Energy band diagrams for the simulated PSCs, showing energy barriers at buffer layer interfaces: (a) PMMA, (b) P3HT, (c) poly-TPD, (d) PTAA, and (e) spiro-OMeTAD.

The analysis identified energy barriers between the HTM and perovskite layer in all simulations, though to varying degrees. The variance in valence band energy levels between the HTM and perovskite layer edge affects device performance. Specifically, energy barriers of -0.1658, -0.4666, -0.1586, -0.1449, and -0.1715 eV were calculated at the maximum power point for PMMA, P3HT, poly-TPD, PTAA, and spiro-OMeTAD, respectively. These energy barriers impede hole transportation from the perovskite layer to the HTM, leading to a decrease in PSCs' performance. Since P3HT had the highest energy barrier, the PSC obtained had the lowest fill factor of 53.22% and the lowest PCE of 16.53%. On the other hand, the calculated energy barriers were smaller in magnitude for other buffer layers. Although one might anticipate that the simulation with poly-TPD would exhibit the smallest energy difference, following a trend of smaller energy barriers with better device performance, the PTAA simulation showed the lowest energy gap. This is mainly attributed to PTAA having a higher relative permittivity,  $\varepsilon_r$ , which modulates the valence band discontinuity at the interface. However, the impact of permittivity on the key performance parameters would be relatively modest in comparison. On the other hand, while spiro-OMeTAD has better power conversion efficiency and closer band alignment with the HTM and perovskite layers, PMMA has a smaller energy barrier. This is due to its very low electron affinity, which creates a large energy gap between the conduction bands at the HTM/buffer layer interface [41]. Consequently, there is a higher electron-hole recombination velocity at the interface, which balances the flow of hole and electron currents and diminishes the measured valence band energy difference. Therefore, although the energy difference in the valence band at interfaces reflects the internal voltage drops and energy barriers resulting from mismatched material properties, its magnitude is dependent on the complex interplay of various factors within a solar cell device. It is only one aspect of a holistic approach to maximizing the overall performance of solar cell devices.

To further understand how band misalignment can result in the appearance of IVDs, the transport equations are invoked [42]:

$$\begin{split} \frac{J_n(x)}{q} &= \mu_n n(x) \frac{dE_{Fc}}{dx} \quad (equation \ 6) \\ \frac{J_p(x)}{q} &= \mu_p n(x) \frac{dE_{Fp}}{dx} \quad (equation \ 7) \end{split}$$

$$\frac{J_p(x)}{a} = \mu_p n(x) \frac{dE_{Fp}}{dx} \quad (equation 7)$$

Where  $\mu_n$  = electron mobility

 $\mu_p$  = hole mobility

n = electron concentration

p = hole concentration

 $J_n$  = current resulting from the flow of electrons

 $J_p$  = current resulting from the flow of holes

 $\mu_n n(x) = electron conductivity$ 

 $\mu_p p(x) = \text{hole conductivity}$ 

To maintain the current flows in the solar cell, there must be a corresponding change in the quasi-Fermi level (qFL) separation. In this context, the hole qFL is highly dependent on the valence band energy alignments at the HTM/buffer layer and buffer layer/perovskite interfaces.

Figure 2(a) is revisited to understand how the performance parameters are affected differently by the formation of IVDs in solar cells using different buffer layer materials. In the initial buffer layer-free solar cell structure, the copper iodide HTM and MALI perovskite exhibit good valence band maximum (VB<sub>max</sub>) alignment of 5.50 and 5.48 eV, respectively. The use of poly-TPD with a VB<sub>max</sub> of 5.34 eV would minimally affect the solar cell's performance parameters, as it still aligns well with the  $VB_{max}$  of the other layers. However, using PMMA (VB<sub>max</sub> = 5.061 eV) would result in the formation of an IVD between the HTM and perovskite layers. This IVD would cause a loss in  $V_{oc}$ , FF, and PCE due to the formation of a transport barrier between the HTM and perovskite layer. The transport barrier arises due to a reduction in hole concentration at the perovskite layer and HTM, near their respective interfaces with the buffer layer. This leads to a decrease in the hole quasi-Fermi level (qFL) to maintain the flow of hole current following the transport equation.

The IVD has minimal impact on the shape of the J-V curve, as its magnitude does not significantly rely on the bias conditions. This is due to the high recombination at the HTM near the interface with the buffer layer, which results in the flow of holes being largely independent of the bias conditions. The IVD is present at  $V_{oc}$  because even though no current flows out of the solar cell, there are still internally balanced electron and hole current flows where the interface recombinations are present. On the other hand, P3HT (VBmax = 5.70) exhibits significantly lower FF results, with  $V_{oc}$  remaining relatively unchanged, as shown in Figure 2(a). In this instance, the IVD forms not at  $V_{oc}$ , but when there is a significant current flow, particularly near the maximum power point, where the absorber experiences a large current flow. Similar to the PMMA case, the majority carrier bottleneck occurs due to a decrease in hole concentration. This time, however, it is located within the buffer layer where a drastic reduction in hole concentration takes place. Correlating with the reduced hole concentration is the increased charge recombination within the buffer layer, resulting in an increase in series resistance, which limits the maximum power point at larger current flows and reduces FF.

#### Thickness of poly-TPD and PSC performance

Figure 4(a)-(b) shows the variations of  $V_{oc}$  and  $J_{sc}$ , FF, and PCE with different poly-TPD buffer layer thicknesses. Error bars (±5% of the y-value range) indicate potential simulation variability across all graphs. The  $V_{oc}$  plots of the thicknesses remain relatively constant. However, a slight increase is observed when reduced to 1 nm and beyond. The graph indicates that  $V_{oc}$  will approach the value of  $V_{oc}$  for the reference buffer layer-free solar cell from a constant 1.2687 V to 1.2700 V. This can be explained by a decrease in volume recombination in the buffer layer, while the light trapping schemes in the photoactive layer remain unchanged [43]. However, the difference in  $V_{oc}$  is only slight, and achieving the  $V_{oc}$  of the buffer layer-free solar cell requires the buffer layer thickness to be vanishingly small.

However, for *J<sub>sc</sub>*, the readings are higher when the thickness of poly-TPD is larger than 1 nm, compared to that of the buffer layer-free solar cell, with a peak observed at 5 nm (24.440994 mA/cm<sup>2</sup>), accompanied by a small trough observed with  $V_{oc}$  (1.2686 V). This may be due to a small increase in electron-hole pair generation within the buffer layer when its thickness is appreciable. This slight increase then drops to a value lower than that of the buffer layerfree solar cell when the thickness is reduced from 5 nm to 1 nm (24.440872 mA/cm<sup>2</sup>). However, beyond this point, when the thickness approaches 0 nm, the *Jsc* increases from the trough at 1 nm to meet that of the buffer layer-free case (24.440920 mA/cm<sup>2</sup>). This is likely because electron-hole pair generation is no longer a dominant factor at these small thicknesses. Instead, Jsc sees an increase due to improved carrier collection, which is contributed to by the shortened distance that carriers need to travel. Unlike  $V_{oc}$ , which remains constant with an increase in thickness beyond 5 nm, Jsc will start to decrease linearly. This corresponds to an increase in series resistance and the distance that charge carriers must travel for extraction [44].

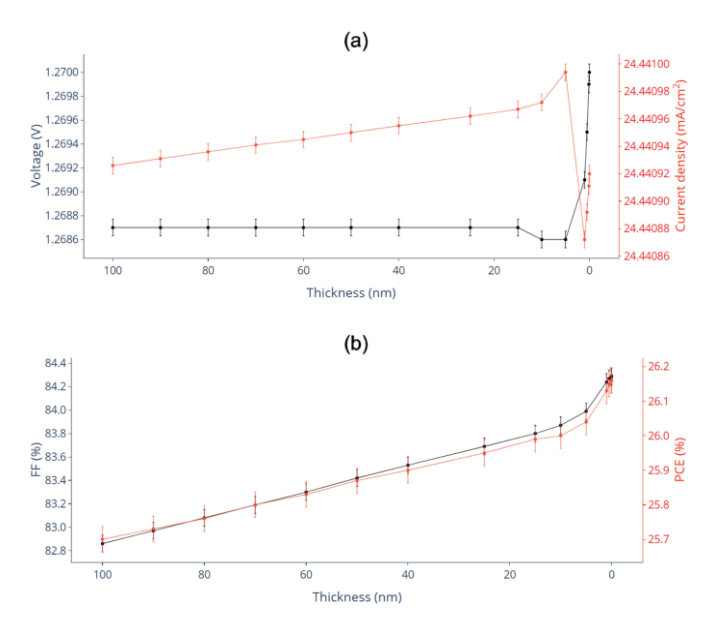


**Figure 4.** (a)  $V_{oc}$  and  $J_{sc}$ , and (b) FF and PCE of the simulated PSCs as a function of poly-TPD thickness.

For *FF* and PCE, the parameters increase somewhat linearly as the buffer layer thickness decreases with a slightly increasing gradient as the thickness approaches 0

nm. A simulation was conducted with a much larger buffer layer thickness of 500 nm, which showed that all performance parameters, except for  $V_{oc}$ , would continue to degrade following the observed trends. To fabricate an optimized solar cell, it is recommended to make the buffer layer thickness as thin as possible within the context of realistic solution processing methods. While simulation software can provide insights into the performance effects of buffer layer thickness, issues such as layer inhomogeneity and reduced device stability may occur in practice. Additionally, it is crucial to minimize the use of expensive polymer materials. It should be noted that the assumption that any thickness of the buffer layer is adequate for protecting the perovskite layer from HTM deposition was made.

### Hole mobility of poly-TPD and PSC performance

In PSCs, high-performance HTMs need high hole mobility for the efficient transfer of photogenerated holes. Research indicates that increased hole mobility leads to an increase in FF [45]. The buffer layer, acting as an interface between the perovskite and HTM, is also critical for hole extraction from the perovskite layer, necessitating high hole mobility. The buffer layer is responsible for facilitating the transport of holes from the perovskite layer to the HTM. Therefore, its hole mobility (µp) should be high to allow efficient transport of holes before they recombine. To study the impact of the buffer layer hole mobility on the PSC performance, the μh of poly-TPD was adjusted from 10<sup>-7</sup> to 40 cm<sup>2</sup> V<sup>-1</sup>s<sup>-1</sup>. Figure 5(a) - (b) illustrates the effect of poly-TPD hole mobility on  $V_{oc}$  and  $J_{sc}$ , and FF and PCE, respectively. While the results show that there are some variations in  $V_{oc}$  and  $J_{sc}$ , these parameters remain relatively constant with changes in  $\mu h$ , particularly in the case of  $V_{oc}$ .  $V_{oc}$  sees a very small increase from 1.2686 to 1.2688 V as the hole mobility of poly-TPD is reduced from 40 to 10<sup>-6</sup> cm<sup>2</sup> V<sup>-1</sup>s<sup>-1</sup>, likely due to an increase in series resistance [46]. Conversely, for Jsc, it is reduced from 24.440972 to 23.945573 mA/cm<sup>2</sup> as μh is made very low (10-7 cm<sup>2</sup> V-1s-1) for a similar reason.

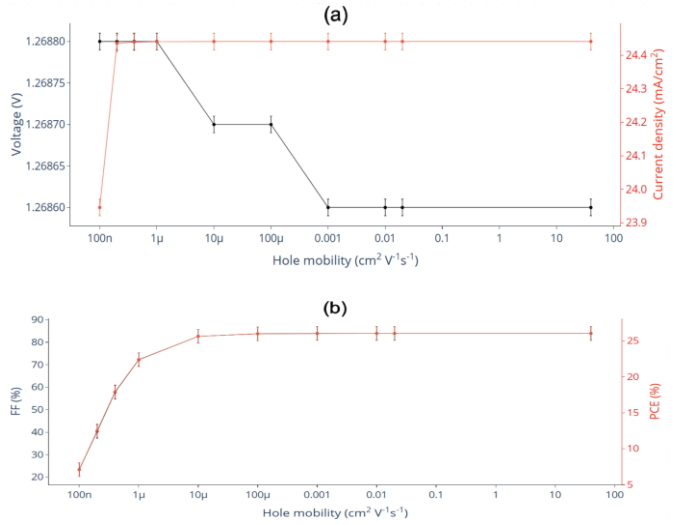


**Figure 5.** (a)  $V_{oc}$  and  $J_{sc}$ , and (b) FF and PCE of the simulated PSCs as a function of poly-TPD hole mobility.

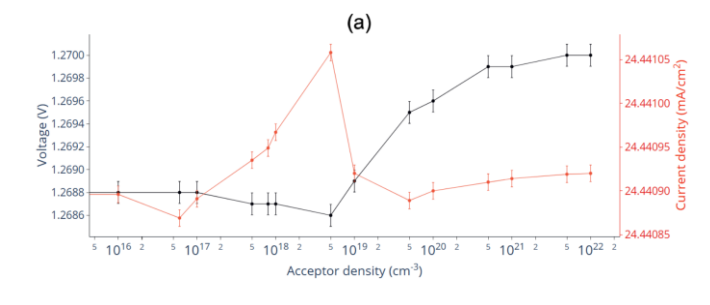
On the other hand, higher values of  $\mu h$  in the buffer layer led to improved hole conduction between the perovskite layer and HTM, resulting in higher FF and PCE. This improvement reaches a plateau around 2 × 10<sup>-2</sup> cm² V<sup>-1</sup>s<sup>-1</sup>, beyond which the performance parameters remain constant, even with increased hole mobility, as long as all other parameters are kept constant. Therefore, to achieve maximum performance, the hole mobility of the poly-TPD buffer layer material only needs to be above approximately 2 × 10<sup>-2</sup> cm² V<sup>-1</sup>s<sup>-1</sup>.

However, it should be noted that this range is specific to materials with the electron affinity and band gap of poly-TPD. Different ranges may be applicable for materials with different energy level profiles. For example, a separate simulation was run for P3HT, where its  $\mu h$  was increased from  $10^{-4}$  cm² V-¹s-¹. With the increase in  $\mu h$ , the greatly reduced FF and PCE were brought back up to match those of the buffer layer-free solar cell. This indicates that the IVD causing the charge carrier bottleneck is a consequence of low  $\mu h$  as well. Poly-TPD would see the best performance as it has both good high  $\mu h$  and good band alignment.

### Acceptor density of poly-TPD and PSC performance

According to a report by Ahmed et al. (2021), p-type doping of HTMs increases positive charges or majority charge carriers, thereby improving the overall conductivity of the HTM and the performance of PSCs [47]. It is expected that this effect would also apply to the buffer layers used in this simulation study, which, like the HTM, extract holes from the perovskite layer. Increasing the Na in the buffer layer may reduce the number of Coulomb traps in the PSC. These traps occur when free charge carriers in the PSC are captured by impurities or defects in the material, resulting in reduced solar cell efficiency. By raising the acceptor density in the buffer layer, the number of available Coulomb traps can be decreased, reducing the chance of free charge carriers being captured and ultimately improving PSC efficiency. To observe the impact of Na on solar cell performance, the Na values were varied between  $10^{16}$  and  $10^{22}$  cm<sup>-3</sup>.

Figure 6(a)-(b) displays the changes in  $V_{oc}$ ,  $J_{sc}$ , FF, and PCE as the Na concentration in the buffer layer varies. It is evident that FF and PCE both increase gradually with Na, but not significantly. A similar trend applies to  $V_{oc}$  and  $I_{sc}$ overall. However, a small peak of higher value (24.441058 mA/cm<sup>2</sup>) is observed at an acceptor density of  $5 \times 10^{18}$  cm<sup>-</sup> <sup>3</sup> for  $J_{sc}$ , while a trough of 1.2686 V is observed for  $V_{oc}$  at the same acceptor density value. The slight deviation of  $V_{oc}$  and J<sub>sc</sub> from the continuously increasing trends of FF and PCE may be due to a slightly higher electron current density observed at this acceptor density value, compared to larger acceptor density values approaching 10<sup>22</sup> cm<sup>-3</sup>. This difference in electron current density observed at the HTM/buffer layer interface may have contributed to an optimal charge carrier balance, resulting in the peak in Isc. However, this observed effect is very small and has no noticeable effect on the increasing trends of FF and PCE with the increase in acceptor density.



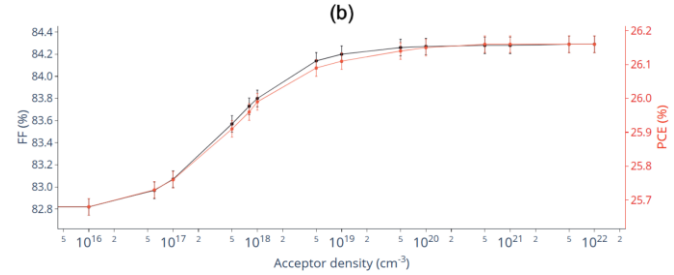


**Figure 6.** (a)  $V_{oc}$  and  $J_{sc}$ , and (b) FF and PCE of the simulated PSCs as a function of poly-TPD acceptor density.

Because the buffer layer is thin, it does not significantly affect the additional electric potential and the built-in electric field between the perovskite layer and the HTM. However, changes in the acceptor concentration of the HTM have a more pronounced effect on the performance parameters of the device.

Even when the  $N_a$  value of the buffer layer drops below  $10^{16}\ cm^{\text{-}3}$ , the performance parameters remain unchanged until  $N_a$  reaches 0 cm $^{\text{-}3}$ . However, when the  $N_a$  value of the HTM falls below a certain threshold, current flow out of the solar cell would cease entirely due to the lack of a built-in electric field to promote charge carrier separation and transportation.

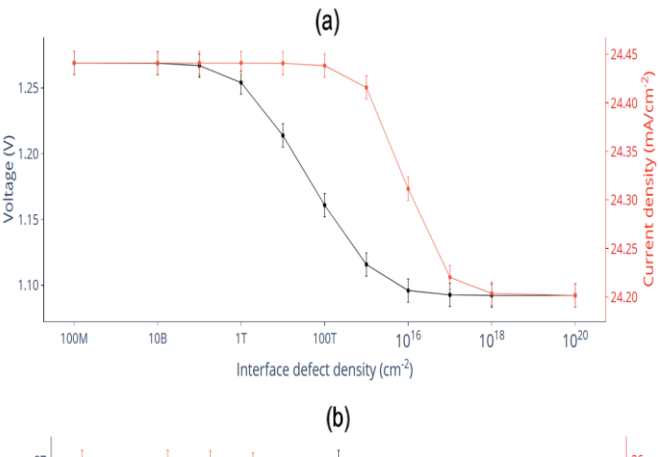
Simulations suggest that the best performance is achieved by setting the  $N_a$  value for the buffer layer as high as possible. However, a  $N_a$  range close to that of the HTM (around  $10^{20}\ \text{cm}^{-3}$ ) produces a comparable performance.

### Interface defect density of poly-TPD and PSC performance

To investigate the effect of buffer layer defect density on device performance, it was varied over the entire allowable range of the simulation software (0 to 10<sup>30</sup> cm<sup>-3</sup>). However, no changes in photovoltaic parameters were observed. The same observation was made when varying the HTM defect density across the same range. This indicates that the trapping of carriers facilitated by defects occurs less in the transporting layers, compared to the perovskite active layer. Previous studies have shown that a high defect density within the perovskite layer is detrimental to device performance [48]. Previous research has discovered that the defect densities at the HTM/perovskite and perovskite/ETM interface layers significantly impact performance parameters. Chouhan et al. (2018) particularly noted that the defect density at the HTM/perovskite interface greatly influences  $V_{oc}$ , while the defect density at the perovskite/ETM interface has a strong effect on the solar cell's  $J_{sc}$  [49].

Since the buffer layer serves as an extension of the HTM to the perovskite layer, the defect density at the buffer layerperovskite layer interface was varied from 10<sup>8</sup> to 10<sup>20</sup> cm<sup>-1</sup> <sup>2</sup>, while the capture cross section for electrons and holes was maintained at 10<sup>-19</sup> cm<sup>2</sup> to observe how it affects solar cell performance. Figure 7(a)-(b) shows respectively the variations of Voc and Jsc, FF, and PCE obtained with different buffer layer (poly-TPD) thicknesses. It is shown that the Voc starts to decrease at an interface defect density of 1010 cm-2 and continues to decline until 1018 cm-2. After this point, the effects level off. Jsc is also affected by an increase in interface defect density, albeit to a lesser degree. This effect is only noticeable at a defect density beyond 1014 cm-2, and it plateaus along with Voc. These findings suggest that the defect density at the buffer layer/perovskite interface primarily affects the Voc by influencing charge recombination and voltage loss mechanisms.

Similarly, the trend of Voc reduction with an increase in interface defect density is followed by PCE. This trend starts and ends at the same point. Interestingly, however, FF increases until it peaks at an interface defect density of 1014 cm-2, after which it decreases along with the other performance parameters. In contrast, the energy difference only increased by 0.25% when measured at the maximum power points of the same curves.



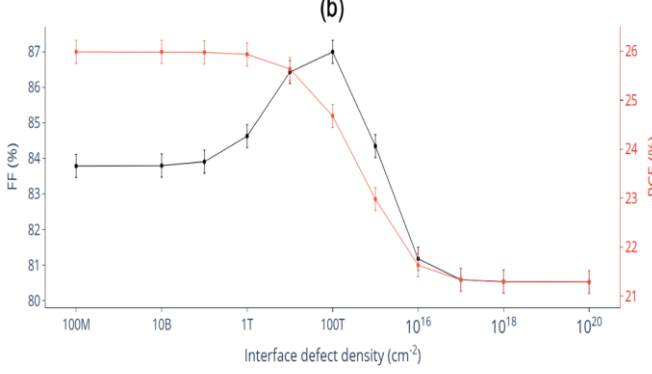


**Figure 7.** (a)  $V_{oc}$  and  $J_{sc}$ , and (b) FF and PCE of the simulated PSCs as a function of poly-TPD/perovskite interface defect density.

However, it should be noted that the increased *FF* does not translate to increased performance, as reflected by the consistently decreasing PCE with increasing interface defect density. When the defect density of the interface exceeds 10<sup>14</sup> cm<sup>-2</sup>, the increased current flowing through

the absorber leads to a decrease in the FF below the simulation with fewer defects. This decrease is due to the rise in series resistance and ideality factor, which negatively impact device performance. Therefore, to optimize the PCE of the device, it is crucial to minimize defect density at the buffer layer/perovskite interface. According to this simulation, the performance parameters at a defect density of  $10^{10} \, \mathrm{cm}^{-2}$  match those of a defect-free device. However, while similar trends can be seen at different defect energy levels and electron and hole capture cross-sections, the ideal defect density values may differ.

### Limitations of the simulation study and future experimental validation

While the simulations offer valuable insights into the performance of buffer layer materials in CuI-based PSCs, several inherent limitations must be acknowledged. The simulations assume homogeneous buffer layers, overlooking potential irregularities during fabrication. Additionally, SCAPS-1D models simplify absorption profiles, failing to capture the complexities observed in experimentally validated perovskite absorption [50].

Furthermore, 1-D modeling cannot fully account for real-world variables, including material defects, light scattering, or textured interfaces. Environmental factors such as moisture, oxygen, and thermal degradation—critical to device performance and stability—are also excluded from the simulations. These necessary simplifications limit the direct applicability of the results to real-world scenarios [51].

Simulation results often tend toward overestimation, partly due to the omission of reflection losses at intermediate interfaces caused by refractive index mismatches [52]. Additionally, assumptions regarding defect density and recombination coefficients—based on limited information in the literature—may underestimate lossy attributes, further skewing the outcomes [53].

To validate the observed trends, future experimental work is essential—particularly through the controlled fabrication of PSCs with varying buffer layers. Techniques such as current-voltage and capacitance-voltage measurements could investigate material and device performance properties [54]. Moreover, photoelectron spectroscopy and time-resolved photoluminescence could provide direct measurements of energy levels and carrier dynamics, further confirming the potential of the poly-TPD buffer layer for enhanced PSC performance [55, 56].

Regarding the stability of the buffer layer or devices, X-ray photoelectron spectroscopy can investigate thermal and moisture-induced reactive pathways [57]. Furthermore, imaging methods like atomic force microscopy could reveal morphological information on the crystallinity of perovskite and CuI layers, as well as their interactions with buffer layers and environmental effects [58].

### 4. CONCLUSION

The simulations identified poly-TPD as the optimal buffer layer material for CuI HTM-based PSCs, based on its

electron affinity and band gap alignment. Tests showed poly-TPD-based PSCs achieved 25.99% PCE, 1.27 V  $V_{oc}$ , 24.44 mA/cm<sup>2</sup>  $J_{sc}$ , and 83.80% FF - superior to PMMA (23.78% PCE), P3HT (16.53% PCE), PTAA (25.90% PCE), and spiro-OMeTAD (25.81% PCE). The buffer layers effectively shield the perovskite layer from CuI solvent damage, with some materials performing notably better than others.

Key performance factors include electron affinity, band gap, and hole mobility of the buffer material. While buffer layers enable practical implementation of CuI and other inorganic HTMs, they don't always improve simulated performance. For best results, the buffer layer should be thin with high hole mobility. Higher acceptor density can boost efficiency, and interface defect density significantly impacts performance.

To confirm the findings of this simulation study, future experimental validation is essential. Experimental investigations could involve fabricating PSCs with varying buffer layers and employing techniques such as currentvoltage and capacitance-voltage measurements to assess device performance properties. Additionally, photoelectron spectroscopy and time-resolved photoluminescence can provide direct insights into energy level alignment and carrier dynamics, validating the proposed advantages of poly-TPD. Stability assessments under environmental conditions, including thermal and moisture-induced stress, are also necessary to evaluate the long-term viability of poly-TPD and similar materials. Imaging methods like atomic force microscopy can further reveal morphological and structural interactions between the buffer layer and perovskite.

These results advance our understanding of efficient PSC development. Proper selection and optimization of buffer layers can enhance PSC performance significantly. However, polymer stability remains a concern, as real-world conditions require materials that withstand temperature and humidity changes. Cost is another limiting factor for commercial adoption.

Future research may also focus on exploring inorganic buffer layer materials that offer greater stability and cost-effectiveness. Candidates such as lead sulfides (PbS), molybdenum oxides (MoO $_{\rm x}$ ), and vanadium oxide (V $_{\rm 2}$ O $_{\rm 5}$ ) are promising due to their high thermal stability, suitable energy level alignment with perovskite layers, and ease of integration into scalable fabrication processes. These materials could potentially provide similar or enhanced performance benefits while addressing the stability and cost challenges associated with organic buffer layers.

#### **ACKNOWLEDGMENTS**

The research was supported by the Ministry of Higher Education (MoHE), through the Fundamental Research Grant Scheme (FRGS/1/2022/TK08/UTAR/02/39).

#### REFERENCES

- [1] J.-P. Correa-Baena et al., "Promises and challenges of perovskite solar cells," *Science*, vol. 358, no. 6364, pp. 739–744, 2017.
- [2] A. S. R. Bati, Y. L. Zhong, P. L. Burn, M. K. Nazeeruddin, P. E. Shaw, and M. Batmunkh, "Next-generation applications for integrated perovskite solar cells," *Commun Mater*, vol. 4, no. 1, p. 2, 2023.
- [3] Y.-E. Lye, K.-Y. Chan, and Z.-N. Ng, "A Review on the Progress, Challenges, and Performances of Tin-Based Perovskite Solar Cells," *Nanomaterials*, vol. 13, no. 3, Art. no. 3, 2023.
- [4] T. M. Brenner, D. A. Egger, L. Kronik, G. Hodes, and D. Cahen, "Hybrid organic—inorganic perovskites: low-cost semiconductors with intriguing charge-transport properties," *Nat Rev Mater*, vol. 1, no. 1, Art. no. 1, 2016.
- [5] H. Zhang, X. Ji, H. Yao, Q. Fan, B. Yu, and J. Li, "Review on efficiency improvement effort of perovskite solar cell," Solar Energy, vol. 233, pp. 421–434, 2022.
- [6] H. Zhang et al., "Improving the stability and performance of perovskite solar cells via off-the-shelf post-device ligand treatment," *Energy Environ. Sci.*, vol. 11, no. 8, pp. 2253–2262, 2018.
- [7] L. Nakka, Y. Cheng, A. G. Aberle, and F. Lin, "Analytical Review of Spiro-OMeTAD Hole Transport Materials: Paths Toward Stable and Efficient Perovskite Solar Cells," *Adv Energy and Sustain Res*, vol. 3, no. 8, p. 2200045, 2022.
- [8] S. Gangala and R. Misra, "Spiro-linked organic small molecules as hole-transport materials for perovskite solar cells," J. Mater. Chem. A, vol. 6, no. 39, pp. 18750– 18765, 2018.
- [9] A. M. N. Abena, A. T. Ngoupo, F. X. A. Abega, and J. M. B. Ndjaka, "Numerical investigation of solar cells based on hybrid organic cation perovskite with inorganic HTL via SCAPS-1D," Chinese Journal of Physics, vol. 76, pp. 94–109, 2022.
- [10] Y. Yang et al., "Spiro-OMeTAD or CuSCN as a preferable hole transport material for carbon-based planar perovskite solar cells," *J. Mater. Chem. A*, vol. 8, no. 25, pp. 12723–12734, 2020.
- [11] S. Sajid, S. Alzahmi, I. B. Salem, and I. M. Obaidat, "Guidelines for Fabricating Highly Efficient Perovskite Solar Cells with Cu2O as the Hole Transport Material," *Nanomaterials*, vol. 12, no. 19, p. 3315, 2022.
- [12] Y.-J. Chen, M.-H. Li, J.-C.-A. Huang, and P. Chen, "Cu/Cu2O nanocomposite films as a p-type modified layer for efficient perovskite solar cells," Sci Rep, vol. 8, no. 1, p. 7646, 2018.
- [13] S. Chaudhary and R. Mehra, "Perovskite solar cell using HTLs copper iodide and spiro-OMeTAD comparative analysis in terms of efficiency and resource utilization," *Appl. Opt.*, vol. 61, no. 1, p. 101, 2022.
- [14] J. Zou et al., "Solvent engineering of LiTFSI towards high-efficiency planar perovskite solar cells," *Solar Energy*, vol. 194, pp. 321–328, 2019.
- [15] M. Srivastava, M. A. Alheity, M. Z. A. Yahya, R. C. Singh, and S. S. Gültekin, "Conduction Mechanism and Photo-

- Electrochemical Performance of Copper Iodide Hole Transport Material-Based Perovskite Solar Cell," *J. Electron. Mater.*, vol. 52, no. 7, pp. 4351–4358, 2023.
- [16] W. Sun *et al.*, "Room-temperature and solution-processed copper iodide as the hole transport layer for inverted planar perovskite solar cells," *Nanoscale*, vol. 8, no. 35, pp. 15954–15960, 2016.
- [17] R. P. Srivastava, H.-S. Jung, and D.-Y. Khang, "Transfer-Printed Cuprous Iodide (CuI) Hole Transporting Layer for Low Temperature Processed Perovskite Solar Cells," *Nanomaterials*, vol. 12, no. 9, p. 1467, 2022.
- [18] M. Burgelman, P. Nollet, and S. Degrave, "Modelling polycrystalline semiconductor solar cells," *Thin Solid Films*, vol. 361–362, pp. 527–532, 2000.
- [19] M. A. Rahman, "Design and simulation of a highperformance Cd-free Cu2SnSe3 solar cells with SnS electron-blocking hole transport layer and TiO2 electron transport layer by SCAPS-1D," *SN Appl. Sci.*, vol. 3, no. 2, p. 253, 2021.
- [20] M. Mostefaoui, H. Mazari, S. Khelifi, A. Bouraiou, and R. Dabou, "Simulation of High Efficiency CIGS Solar Cells with SCAPS-1D Software," Energy Procedia, vol. 74, pp. 736–744, 2015.
- [21] R. K. Yadav et al., "A qualitative study of SnSe thin film solar cells using SCAPS 1D and comparison with experimental results: A pathway towards 22.69% efficiency," Solar Energy Materials and Solar Cells, vol. 244, p. 111835, 2022.
- [22] W. Abdelaziz, A. Zekry, A. Shaker, and M. Abouelatta, "Numerical study of organic graded bulk heterojunction solar cell using SCAPS simulation," Solar Energy, vol. 211, pp. 375–382, Nov. 2020.
- [23] S. Karthick, S. Velumani, and J. Bouclé, "Experimental and SCAPS simulated formamidinium perovskite solar cells: A comparison of device performance," *Solar Energy*, vol. 205, pp. 349–357, 2020.
- [24] M. M. Salah, M. Abouelatta, A. Shaker, K. M. Hassan, and A. Saeed, "A comprehensive simulation study of hybrid halide perovskite solar cell with copper oxide as HTM," Semicond. Sci. Technol., vol. 34, no. 11, p. 115009, 2019.
- [25] M. Dadashbeik, D. Fathi, and M. Eskandari, "Design and simulation of perovskite solar cells based on graphene and TiO2/graphene nanocomposite as electron transport layer," *Solar Energy*, vol. 207, pp. 917–924, 2020.
- [26] A. B. Coulibaly, S. O. Oyedele, N. R. Kre, and B. Aka, "Comparative Study of Lead-Free Perovskite Solar Cells Using Different Hole Transporter Materials," MNSMS, vol. 09, no. 04, pp. 97–107, 2019.
- [27] N. Kumar, R. J. Sengwa, P. Dhatarwal, and M. Saraswat, "Effectively polymer composition controllable optical properties of PVDF/PMMA blend films for advances in flexible device technologies," *IJEMS*, vol. 29, no. 02, 2022.
- [28] S. M. Sayyah, A. B. Khaliel, and H. Moustafa, "Electronic Structure and Ground State Properties of PMMA Polymer: I. Step-By-Step Formation and Stereo-Regularity of the Polymeric Chain—AM1-MO

- Treatment," *International Journal of Polymeric Materials*, vol. 54, no. 6, pp. 505–518, 2005.
- [29] U. Abaci, H. Y. Guney, and M. Yilmazoglu, "Plasticizer effect on dielectric properties of poly(methyl methacrylate)/titanium dioxide composites," *Polymers and Polymer Composites*, vol. 29, no. 9\_suppl, pp. S565–S574, 2021.
- [30] E. Karimi and S. M. B. Ghorashi, "Simulation of perovskite solar cell with P 3 HT hole-transporting materials," J. *Nanophoton*, vol. 11, no. 3, p. 032510, 2017.
- [31] A. Intaniwet, C. A. Mills, P. J. Sellin, M. Shkunov, and J. L. Keddie, "Achieving a Stable Time Response in Polymeric Radiation Sensors under Charge Injection by X-rays," *ACS Appl. Mater. Interfaces*, vol. 2, no. 6, pp. 1692–1699, 2010.
- [32] E. Akman and S. Akin, "Poly(N, N'-bis-4-butylphenyl-N, N'-bisphenyl)benzidine-Based Interfacial Passivation Strategy Promoting Efficiency and Operational Stability of Perovskite Solar Cells in Regular Architecture," *Adv. Mater.*, vol. 33, no. 2, p. 2006087, 2021.
- [33] H.-J. Du, W.-C. Wang, and J.-Z. Zhu, "Device simulation of lead-free CH 3 NH 3 SnI 3 perovskite solar cells with high efficiency," *Chinese Phys. B*, vol. 25, no. 10, p. 108802, 2016.
- [34] G. A. Casas, M. A. Cappelletti, A. P. Cédola, B. M. Soucase, and E. L. Peltzer Y Blancá, "Analysis of the power conversion efficiency of perovskite solar cells with different materials as Hole-Transport Layer by numerical simulations," *Superlattices and Microstructures*, vol. 107, pp. 136–143, 2017.
- [35] F. Baig, "Numerical analysis for efficiency enhancement of thin film solar cells.," Universitat Politècnica de València, Valencia (Spain), 2019.
- [36] D. Zhao, M. Sexton, H. Park, G. Baure, J. C. Nino, and F. So, "High-Efficiency Solution-Processed Planar Perovskite Solar Cells with a Polymer Hole Transport Layer," *Advanced Energy Materials*, vol. 5, no. 6, p. 1401855, 2015.
- [37] Z. Safari *et al.*, "Optimizing the Interface between Hole Transporting Material and Nanocomposite for Highly Efficient Perovskite Solar Cells," *Nanomaterials*, vol. 9, no. 11, p. 1627, 2019.
- [38] J. Höcker, D. Kiermasch, P. Rieder, K. Tvingstedt, A. Baumann, and V. Dyakonov, "Efficient Solution Processed CH<sub>3</sub> NH<sub>3</sub> PbI<sub>3</sub> Perovskite Solar Cells with PolyTPD Hole Transport Layer," Zeitschrift für Naturforschung A, vol. 74, no. 8, pp. 665–672, 2019.
- [39] M. Ahsan Saeed, S. Hyeon Kim, K. Baek, J. K. Hyun, S. Youn Lee, and J. Won Shim, "PEDOT:PSS: CuNW-based transparent composite electrodes for high-performance and flexible organic photovoltaics under indoor lighting," *Applied Surface Science*, vol. 567, p. 150852, 2021.
- [40] S. H. Kim, C. H. Park, M. A. Saeed, D.-H. Ko, J.-H. Lee, and J. W. Shim, "β-cyclodextrin-polyacryloyl hydrazidebased surface modification for efficient electroncollecting electrodes of indoor organic photovoltaics,"

- *Journal of Materials Research and Technology*, vol. 16, pp. 1659–1666, 2022.
- [41] M. N. Zidan, N. Everitt, T. Ismail, and I. S. Fahim, "Organic Solar Cells Parameters Extraction and Characterization Techniques," *Polymers*, vol. 13, no. 19, p. 3224, 2021.
- [42] N. Wu et al., "Identifying the Cause of Voltage and Fill Factor Losses in Perovskite Solar Cells by Using Luminescence Measurements," *Energy Technol.*, vol. 5, no. 10, pp. 1827–1835, 2017.
- [43] G. Smestad and H. Ries, "Luminescence and current-voltage characteristics of solar cells and optoelectronic devices," *Solar Energy Materials and Solar Cells*, vol. 25, no. 1–2, pp. 51–71, 1992.
- [44] N. Mundhaas et al., "Series Resistance Measurements of Perovskite Solar Cells Using J sc V oc Measurements," *Solar RRL*, vol. 3, no. 4, p. 1800378, 2019.
- [45] L. M. Cavinato, E. Fresta, S. Ferrara, and R. D. Costa, "Merging Biology and Photovoltaics: How Nature Helps Sun-Catching," *Advanced Energy Materials*, vol. 11, no. 43, p. 2100520, 2021.
- [46] A. Sunny and S. R. A. Ahmed, "Numerical Simulation and Performance Evaluation of Highly Efficient Sb 2 Se 3 Solar Cell with Tin Sulfide as Hole Transport Layer," *Physica Status Solidi (b)*, vol. 258, no. 7, p. 2000630, 2021.
- [47] S. Ahmed, F. Jannat, Md. A. K. Khan, and M. A. Alim, "Numerical development of eco-friendly Cs2TiBr6 based perovskite solar cell with all-inorganic charge transport materials via SCAPS-1D," *Optik*, vol. 225, p. 165765, 2021.
- [48] S. Mahjabin et al., "Perceiving of Defect Tolerance in Perovskite Absorber Layer for Efficient Perovskite Solar Cell," *IEEE Access*, vol. 8, pp. 106346–106353, 2020.
- [49] A. S. Chouhan, N. P. Jasti, and S. Avasthi, "Effect of interface defect density on performance of perovskite solar cell: Correlation of simulation and experiment," *Materials Letters*, vol. 221, pp. 150–153, 2018.

- [50] P. Basumatary and P. Agarwal, "Two-step fabrication of MAPbI perovskite thin films with improved stability," *Bull Mater Sci*, vol. 42, no. 6, p. 268, 2019.
- [51] M. Topič, M. Sever, B. Lipovšek, A. Čampa, and J. Krč, "Approaches and challenges in optical modelling and simulation of thin-film solar cells," *Solar Energy Materials and Solar Cells*, vol. 135, pp. 57–66, 2015.
- [52] M. Burgelman, K. Decock, A. Niemegeers, J. Verschraegen, and S. Degrave, "SCAPS Manual, Version: 23." Department of Electronics and Information Systems (ELIS) of the University of Gent, Belgium, 2018.
- [53] A. Saidarsan, S. Guruprasad, A. Malik, P. Basumatary, and D. S. Ghosh, "A critical review of unrealistic results in SCAPS-1D simulations: Causes, practical solutions and roadmap ahead," Solar Energy Materials and Solar Cells, vol. 279, p. 113230, 2025.
- [54] I. M. Dharmadasa, Y. Rahaq, A. A. Ojo, and T. I. Alanazi, "Perovskite solar cells: a deep analysis using current-voltage and capacitance-voltage techniques," *J Mater Sci: Mater Electron*, vol. 30, no. 2, pp. 1227–1235, 2019.
- [55] Y. Yamano, T. Tani, and T. Uchida, "Characterization of Hole Transport Layer in Perovskite Solar Cell via Its Performance and Electronic Structure," *The Society of Photography and Imaging of Japan*: 2. 2019.
- [56] E. V. Péan, S. Dimitrov, C. S. De Castro, and M. L. Davies, "Interpreting time-resolved photoluminescence of perovskite materials," *Phys. Chem. Chem. Phys.*, vol. 22, no. 48, pp. 28345–28358, 2020.
- [57] F. Baumann, S. R. Raga, and M. Lira-Cantú, "Monitoring the stability and degradation mechanisms of perovskite solar cells by *in situ* and *operando* characterization," *APL Energy*, vol. 1, no. 1, p. 011501, 2023.
- [58] D. Cui *et al.*, "Color-Tuned Perovskite Films Prepared for Efficient Solar Cell Applications," *J. Phys. Chem. C*, vol. 120, no. 1, pp. 42–47, 2016.